arXiv:1908.02372v1 [astro-ph.GA] 6 Aug 2019

A dominant population of optically invisible massive galaxies in the early Universe

T. Wang[1,2,3], C. Schreiber[4,5,6], D. Elbaz[2], Y. Yoshimura[1], K. Kohno[1,6], X. Shu[7], Y. Yamaguchi[1], M. Pannella[8], M. Franco[2], J. Huang[9], C.-F. Lim[10,11] & W.-H. Wang[10]

[1]Institute of Astronomy, Graduate School of Science, The University of Tokyo, Tokyo, Japan [2]AIM, CEA, CNRS, Université Paris Diderot, Saclay, Sorbonne Paris Cité, Gif-sur-Yvette, France [3]National Astronomical Observatory of Japan, Mitaka, Tokyo, Japan [4]Leiden Observatory, Leiden University, Leiden, The Netherlands [5]Department of Physics, University of Oxford, Oxford, UK [6]Research Center for the Early Universe, Graduate School of Science, Tokyo, Japan [7]Department of Physics, Anhui Normal University, Wuhu, China [8]Faculty of Physics, Ludwig-Maximilians-Universität, Munich, Germany [9]National Astronomical Observatories of China, Chinese Academy of Sciences, Beijing, China [10]Academia Sinica Institute of Astronomy and Astrophysics, Taipei,, Taiwan [11]Graduate Institute of Astrophysics, National Taiwan University, Taipei, Taiwan

Our current knowledge of cosmic star-formation history during the first two billion years (corresponding to redshift $z > 3$) is mainly based on galaxies identified in rest-frame ultraviolet light[1]. However, this population of galaxies is known to under-represent the most massive galaxies, which have rich dust content and/or old stellar populations. This raises the questions of the true abundance of massive galaxies and the star-formation-rate density in the early universe. Although several massive galaxies that are invisible in the ultraviolet have recently been confirmed at early epochs[2,3,4], most of them are extreme starbursts with star-formation rates exceeding 1000 solar masses per year, suggesting that they are unlikely to represent the bulk population of massive galaxies. Here we report submillimeter (wavelength 870 μm) detections of 39 massive star-forming galaxies at $z > 3$, which are unseen in the spectral region from the deepest ultraviolet to the near-infrared. With a space density of about 2×10^{-5} per cubic megaparsec (two orders of magnitudes higher than extreme starbursts[5]) and star-formation rates of ~200 solar masses per year, these galaxies represent the bulk population of massive galaxies that have been missed from previous surveys. They contribute a total star-formation- rate density ten times larger than that of equivalently massive ultraviolet-bright galaxies at $z > 3$. Residing in the most massive dark matter halos at their redshifts, they are probably the progenitors of the largest present-day galaxies in massive groups and clusters. Such a high abundance of massive and dusty galaxies in the early universe challenges our understanding of massive-galaxy formation.

Observations of galaxies across cosmic time have revealed that more massive galaxies have assembled their stellar masses at earlier epochs, with a significant population of massive ellipticals already in place at redshifts $z \sim 3-4$[6,7,8]. The early assembly of these massive galaxies has posed serious challenges to current galaxy formation theories. Understanding their formation processes requires studies of their progenitors formed at even higher redshifts. However, most currently known high-redshift galaxies, including mainly Lyman-break galaxies (LBGs) and few extreme starbursts, are found inadequate to account for the large population of these early formed ellipticals, due to either low stellar masses and star formation rates, SFRs (for LBGs[9]) or low space densities (for the extreme starbursts). This suggests that the main progenitors of massive galaxies at $z > 3$ remain to be found. Identification of these currently missing massive galaxies is key to our understanding of both massive-galaxy formation and the cosmic SFR density in the early universe.

The main targets of this study are a population of galaxies that are *Spitzer*/Infrared Array Camera (IRAC)-bright yet undetected in even the deepest near-infrared (NIR: H-band) imaging with Hubble Space Telescope (*HST*), that is, H-dropouts. (Throughout this Letter we use the short form "Telescope/Instrument" to represent usage of a particular instrument on a particular telescope.) In total, we have identified 63 $H-$dropouts with IRAC 4.5-μm magnitude, [4.5], less than 24 mag, within a total survey area of $\sim$ 600 arcmin^2 in deep CANDELS fields with typical depth of $H > 27$ mag (5σ)(Fig. 1, Extended Data Table 1, Methods). Although previous studies have shown that these bright and red IRAC sources are promising candidates for massive galaxies at[10,11] $z > 3$, confirming their nature has been difficult so far owing to the limited sample size, the poor resolution of *Spitzer* and the lack of multiwavelength information. Here we explore their nature with high-resolution, 870 μm continuum imaging with the Atacama Large Millimeter/submillimeter Array (ALMA). With only 1.8 min of integration per object, 39 of them (detection rates of 62%) are detected down to an integrated flux of 0.6 mJy (4σ, Extended Data Fig. 1, Extended Data Table 2). Their 870-μm fluxes range from 0.6 mJy to 8 mJy, with a median of $S_{870\ \mu m}$ =1.6 mJy (Extended Data Fig. 2). Hence most of them are fainter than the 2-mJy confusion limit of the single dish instruments that discovered submillimeter galaxies (SMGs), and much fainter than most SMGs studied until now with typical[12] $S_{870\ \mu m} \gtrsim 4$ mJy. The sky density of these ALMA-detected H-dropouts is approximately 5.3×10^2 deg^{-2} after correction for incompleteness (Methods), two orders of magnitude higher than *Herschel*/SPIRE-selected extreme starbursts (with SFR $\gtrsim 1000\ M_\odot$ yr^{-1})[3,5].

The ALMA detections confirm unambiguously that most of the H-dropouts are dusty star-forming galaxies at high redshifts, consistent with their admittedly uncertain photometric redshifts–from optical spectral energy distribution (SED) fitting–with median redshift $z_{\rm median} = 4$ (Extended Data Fig. 3). Further insights into their properties are obtained from the stacked infrared (IR) SED of the 39 ALMA-detected H-dropouts from MIPS 24 μm up to ALMA 870 μm. The stacked SED peaks between the observed 350 and 500 μm (Extended Data Figure 3), consistent with being at $z \sim 4$. With a median stellar mass of $M_* \sim 10^{10.6} M_\odot$ and a characteristic IR luminosity (over $8-1000\ \mu$m) of $L_{IR} = 2.2 \pm 0.3 \times 10^{12} L_\odot$ ($L_\odot$, solar luminosity) derived from the stacked SED, these ALMA-detected H-dropouts are fully consistent with being normal massive star-forming galaxies at[13] $z = 4$ (Fig. 2). Moreover, the ALMA detections also provide crucial constrains on the redshift of individual galaxies. Combined with SCUBA-2 450 μm and VLA 3 GHz data, the majority of the ALMA-detected H-dropouts exhibit red $S_{870\mu m}/S_{450\mu m}$ and $S_{1.4GHz}/S_{870\mu m}$ colors that are suggestive of redshifts of $z > 3$ (Extended Data Fig. 4). Similarly,

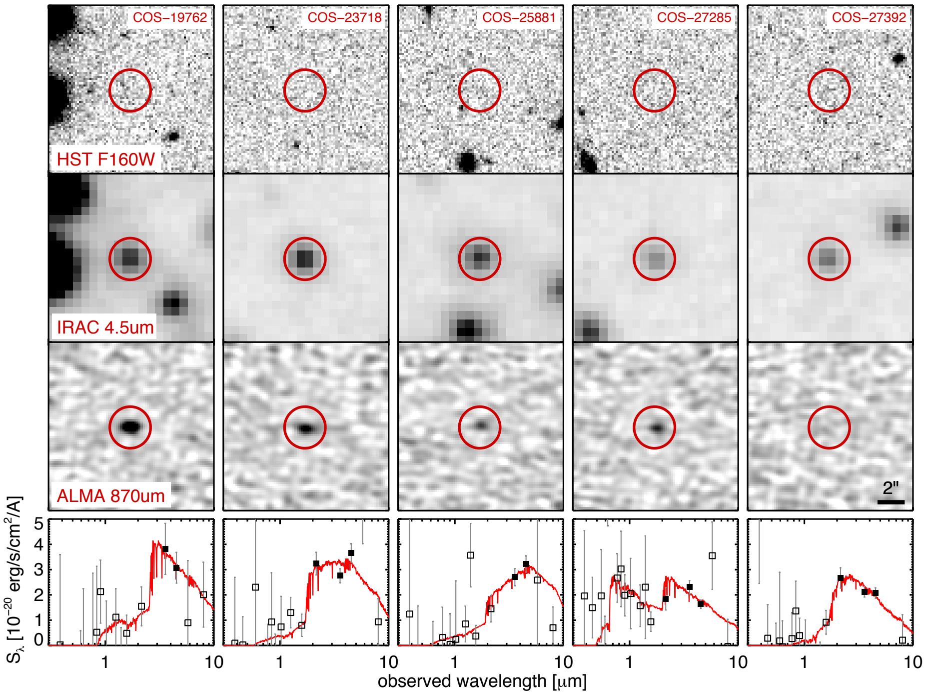

Figure 1 | Example images and UV-to-NIR SEDs of H-dropouts. Top three rows, images of five H-dropouts obtained in three different spectral bands-HST/F160W (top row), IRAC 4.5 μm (second row), and ALMA 870 μm (third row). The H-dropouts, named in the top row, were selected randomly from the parent sample, with all but the last one (COS-27392) detected with ALMA. Each image is 12″ × 12″; see scale bar in bottom right image. Bottom row, the measured UV-to-NIR SED (squares) and best-fit stellar population synthesis models (red lines). The error bars are 1 σ. The filled and open squares indicate photometric points with measured signal-to-noise ratio (S/N) above and below 3, respectively.

the non-detections at 24 μm (5σ detection limit of 20 μJy) for most of the sources implies red $S_{870\ \mu m}/S_{24\mu m}$ colors that are also consistent with $z > 3$ assuming typical SED templates[14]. We hence conclude that whereas the estimated redshifts for individual galaxies exhibit a large uncertainty, all the available data points to the ALMA-detected H-dropouts being massive, dusty star-forming galaxies at $z > 3$.

For the remaining approximately 40% of H-dropouts that are not detected with ALMA, photometric redshift estimates based on their optical SEDs suggest a similar redshift distribution to that of ALMA-detected ones, with $z_{\rm median} = 3.8$(Extended Data Figure 2). Their stacked ALMA 870 μm image yields a 6σ detection with $S_{870\mu m} = 0.24 \pm 0.04$ mJy, approximately 8 times lower than that of ALMA-detected ones, suggesting lower specific SFRs compared to ALMA-detected ones, which is also confirmed by a full fitting of the stacked optical-to-IR SEDs (Extended Data Fig. 5).

Spectroscopic confirmation of H-dropouts has been so far limited to a few sources, which are all found at $z > 3$. Most of these confirmed cases are extreme SMGs with $S_{870\mu m} \gtrsim 10$ mJy, for example[2]., $HDF - 850atz = 5.18$. An H-dropout galaxy with submillimeter flux similar to that of our sample ($S_{744\mu m} = 2.3 \pm 0.1$ mJy) has been recently confirmed[15] to be at $z = 3.709$: it was discovered serendipitously near a quiescent galaxy at the same redshift[6]. By targeting 3 H-dropouts in our sample that show significant excess ($> 4\sigma$, Methods) in Subaru medium bands in the optical (~ 3500-6000 Å) with VLT/X-shooter, we have successfully detected Lyman-α for two of them and confirmed their redshifts to be $z > 3$ ($z = 3.097$ and $z = 5.113$, Extended Data Fig. 6). These spectroscopic redshifts ($z_{\rm spec}$ are in good agreement with their photometric redshift ($z_{\rm phot}$) based on UV-to-NIR SED fitting, with $\sigma_{\Delta z/(1+z_{spec})} \sim 0.1$.

Having established that most of the H-dropouts are massive galaxies at $z > 3$, we now derive their contribution to the cosmic SFR density and stellar mass function. Whereas populations of similarly red galaxy

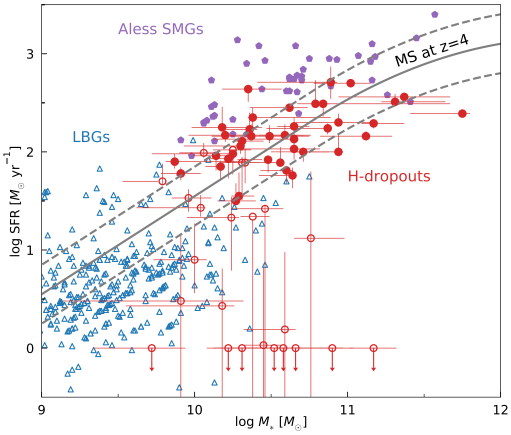

Figure 2 | Stellar masses and star formation rates of H-dropouts. The red filled and open circles represent respectively the ALMA-detected and ALMA-undetected H−dropouts. For comparison, a sample of LBGs at $z = 4 - 6$ from the ZFOURGE survey[22] and bright $z > 3$ SMGs ($S_{870\mu m} > 4.2$ mJy) from the ALESS survey are also shown[23]. The stellar masses for the ALESS SMGs are reduced by 0.3 dex to account for the systematic differences caused by the different methods used in mass estimation. The grey solid and dashed lines indicate respectively the star-forming main sequence (MS) at $z = 4$ and its 1σ scatter[24]. The SFRs for ALMA-detected H-dropouts are derived from the 870-μm fluxes assuming their intrinsic far-infrared SED resembles that of the stacked one. Error bars are 1σ. The SFRs for ALMA-undetected H-dropouts are derived from UV-to-NIR SED fitting with an additional constraint of SFR > 1 $M_\odot$ yr^{-1}, for which error bars represent the 16th and 84th percentiles of the distribution obtained in the Monte Carlo simulations (Methods), the same as that for stellar mass estimates.

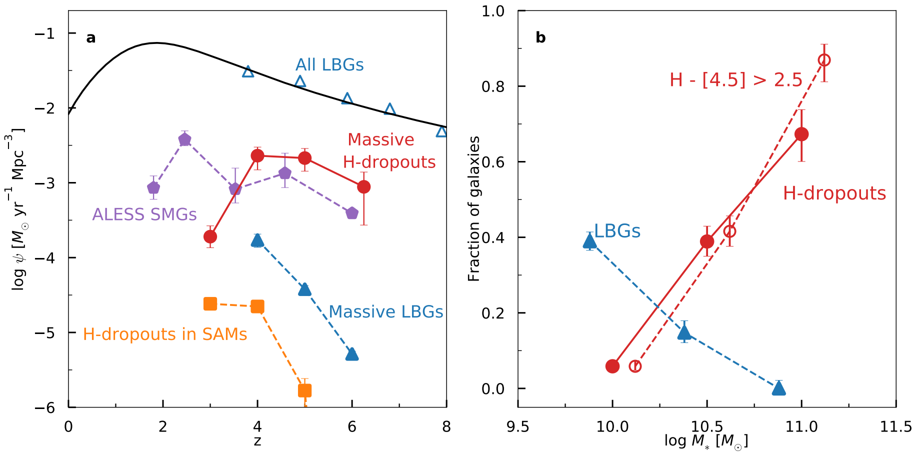

Figure 3 | Contribution of H-dropouts to the cosmic SFR density and the stellar mass function. a: Plot of cosmic star-formation-rate density, ψ, versus redshift z. The black line indicates the current known total cosmic star-formation history, which is based on LBGs at $z \gtrsim 4$ ('All LBGs', blue open triangles[17]). Red filed circles ('Massive H-dropouts'), ALMA-detected H-dropouts with $M_* > 10^{10.3} M_\odot$. Purple fileld pentagons, the ALESS SMGs ($S_{870\mu m} > 4.2$ mJy)[12], whose contribution to the SFR density peaks at $z \approx 2.5$. Blue filled triangles ('Massive LBGs'), the SFR density (based on dust-corrected UV) for the brightest/massive LBGs with $M_* > 10^{10.3} M_\odot$, based on the latest determination of the UV luminosity functions[25]. Filled orange squares, the SFR density from H-dropouts ($[4.5] < 24$ and $H - [4.5] > 2.5$) in semi-analytical models[19], which are identified from a K-selected mock catalog ($K < 27$) from a total area of 75.36 deg^2. Error bars, s.d. assuming Poisson statistics. **b**: Number fraction of massive galaxies from the H-dropout sample and ZFOURGE catalogues that are detected either as LBGs (blue filled triangles) or H-dropouts (including both ALMA-detected and ALMA-undetected ones; red filled circles) averaged over $z = 3.5 - 6.5$. Red open circles, the total contribution of red galaxies, including both H-dropouts and those non-H-dropouts that have similar red colors ($H - [4.5] > 2.5$) selected from ZFOURGE at $3.5 < z < 6.5$.

populations are known to exist at lower redshifts[16], these largely overlap with the stellar-mass-limited sample used to estimate the SFR density at $z < 3$. Assuming that the intrinsic infrared SED of the ALMA-detected H-dropouts is the same as the SED derived from stacking, the SFR density of ALMA-detected H-dropouts (in $10^{-3} M_\odot$ yr^{-1} Mpc^{-3}) reaches about 2.9, 2.1, and 0.9 at $z = 4, 5, 6$, respectively, or approximately $1.6{\times}10^{-3} M_\odot$ yr^{-1} Mpc^{-3} when averaged over the three bins (Fig. 3). This corresponds to about 10% of the SFR density from LBGs at similar redshifts[17]. However, if we focus only on LBGs with masses similar to those of $H-$dropouts with $M_* > 10^{10.3} M_\odot$, the SFR densities of $H-$dropouts are one to two orders of magnitude higher, demonstrating that H-dropouts dominate the SFR density in massive galaxies. This dominance is further reflected in the stellar mass functions, as shown in Fig. 3. The fraction of H-dropout becomes progressively higher at higher masses. At $M_* \gtrsim 10^{10.5} M_\odot$, the number density of H-dropout surpasses that of LBGs. Moreover, if we also include galaxies detected in $H-$band but which show similar red colors ($H - [4.5] > 2.5$, Extended Data Fig. 7)[8,11], they make up more than than 80% of the most massive galaxies at $z > 4$. Taken together, these results suggest that the majority of the most massive galaxies at $z > 3$ have indeed been missed from the LBG selection, and are optically dark.

To put the H-dropouts in the context of the cosmic evolution of massive galaxies, we probe their clustering properties through their cross-correlation with H-detected galaxies at $3.5 < z < 5.5$ from the CANDELS survey in the same three fields (Extended Data Fig. 8, Methods). The derived galaxy bias, that is, the relationship between the spatial distribution of galaxies and the underlying dark matter density field, for the H-dropouts is $b = 8.4 \pm 1.5$, corresponding to a dark matter halo mass of $M_\mathrm{h} \sim 10^{13\pm0.3} h^{-1} M_\odot$ at $z = 4$ (Fig. 4, Methods). This halo mass of H-dropouts is consistent with them being progenitors of the most massive quiescent galaxies at $z = 2 - 3$, as well as progenitors of today's ellipticals that reside in the central region of massive groups and clusters.

The discovery and confirmation of these H-dropouts as massive galaxies at $z \approx 3 - 6$ alleviates greatly the tension between the small number of massive LBGs at $z > 3$ and the rapid emergence of massive

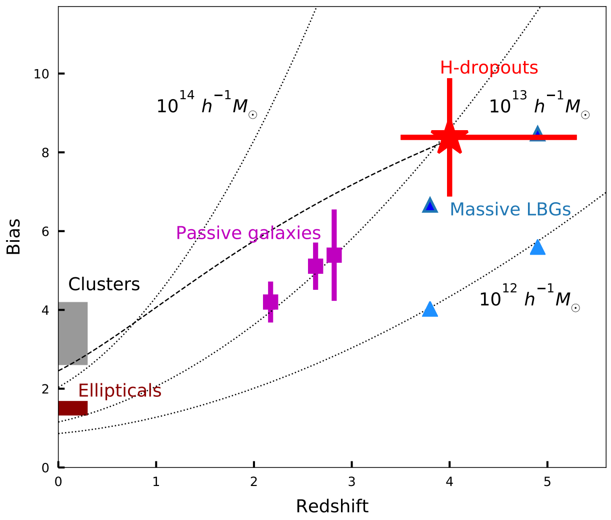

Figure 4 | Clustering properties and halo masses of H-dropouts. Shown is the galaxy bias of ALMA-detected H-dropouts (red star) and its comparison to other populations, including the brightest LBGs ('Massive LBGs'; blue triangles) at $z \sim 4 - 5$ (ref.[26]), massive passive galaxies ('Passive galaxies': purple squares) with $M_* > 10^{10.5} M_\odot$ at $z = 2 - 3$ (ref.[27]), local massive ellipticals with $L = 2 - 4L_*$ ('Ellipticals'; dark-red-shaded region) and clusters ('Clusters'; grey-shaded region). Error bars, 1σ estimated from Poisson statistics. Filled dark-blue and light-blue triangles denote massive and more typical (L_*) LBGs with UV magnitudes of $M_{UV} \approx -22$ and $M_{UV} \approx -20.5$, respectively. Dotted lines, the corresponding galaxy bias for fixed halo mass (labelled) at different redshifts[28]; dashed line, the evolutionary track[29] for galaxies with the same galaxy bias as H-dropouts. The descendants of H-dropouts are consistent with massive ellipticals at $z \sim 2 - 3$ and today's most massive galaxies residing in massive groups and clusters.

(and quiescent) galaxies at $z \approx 2-3$. Assuming an average redshift of $z \approx 4$ and SFR $\approx 220\ M_{\odot}\ \mathrm{yr}^{-1}$, these H-dropouts will grow in stellar mass by $1.3 \times 10^{11} M_{\odot}$ before $z \sim 3$. Their number density, $n \sim 2 \times 10^{-5}$ Mpc^{-3}, is also comparable to that of the most massive, quiescent galaxies at $z \sim 3$ with[18] $M_* > 10^{11} M_{\odot}$. The early formation of such a large number of massive, dusty galaxies is unexpected with current semi-analytical models[19], which underestimates their density by one to two orders of magnitude (Fig. 3). Similarly, a deficit of such galaxies is also present in hydrodynamic simulations, which contain no such galaxies at $z > 3$ in mock deep fields ($\sim$ 23.5 arcmin^2) from the Illustris Project[20]. Moreover, even considering LBGs alone, the number of massive galaxies already appears too large when compared to the number of massive halos at $z > 4$ predicted[21] by our current understanding of galaxy evolution in the Lambda Cold Dark Matter (LCDM) framework. Together, this unexpected large abundance of massive galaxies in the early Universe suggests that our understanding of massive-galaxy formation may require substantial revision. Spectroscopic follow-up of the whole population of H-dropouts would be key to providing further insights into this question, which calls for mid-infrared spectroscopy with James Webb Space Telescope in the near future.

1. Madau, P. & Dickinson, M. Cosmic Star-Formation History. *Annu. Rev. Astron. Astrophys.* **52**, 415–486 (2014).
2. Walter, F. *et al.* The intense starburst HDF 850.1 in a galaxy overdensity at z ≈5.2 in the Hubble Deep Field. *Nature* **486**, 233–236 (2012).
3. Riechers, D. A. *et al.* A dust-obscured massive maximum-starburst galaxy at a redshift of 6.34. *Nature* **496**, 329–333 (2013).
4. Marrone, D. P. *et al.* Galaxy growth in a massive halo in the first billion years of cosmic history. *Nature* **553**, 51–54 (2018).
5. Dowell, C. D. *et al.* HerMES: Candidate High-redshift Galaxies Discovered with Herschel/SPIRE. *Astrophys. J.* **780**, 75 (2014).
6. Glazebrook, K. *et al.* A massive, quiescent galaxy at a redshift of 3.717. *Nature* **544**, 71–74 (2017).
7. Schreiber, C. *et al.* Near infrared spectroscopy and star-formation histories of 3 ≤ z ≤ 4 quiescent galaxies. *Astron. Astrophys.* **618**, A85 (2018).
8. Spitler, L. R. *et al.* Exploring the z = 3-4 Massive Galaxy Population with ZFOURGE: The Prevalence of Dusty and Quiescent Galaxies. *Astrophys. J. Let.* **787**, L36 (2014).
9. Williams, C. C. *et al.* The Progenitors of the Compact Early-type Galaxies at High Redshift. *Astrophys. J.* **780**, 1 (2014).
10. Huang, J.-S. *et al.* Four IRAC Sources with an Extremely Red H - [3.6] Color: Passive or Dusty Galaxies at z ¿ 4.5? *Astrophys. J. Let.* **742**, L13 (2011).
11. Wang, T. *et al.* Infrared Color Selection of Massive Galaxies at z > 3. *Astrophys. J.* **816**, 84 (2016).
12. Swinbank, A. M. *et al.* An ALMA survey of sub-millimetre Galaxies in the Extended Chandra Deep Field South: the far-infrared properties of SMGs. *Mon. Not. R. Astron. Soc.* **438**, 1267–1287 (2014).
13. Schreiber, C. *et al.* Dust temperature and mid-to-total infrared color distributions for star-forming galaxies at 0 < z < 4. *Astron. Astrophys.* **609**, A30 (2018).
14. Daddi, E. *et al.* Two bright submillimeter galaxies in a z = 4.05 protocluster in GOODS-North, and accurate radio-infrared photometric redshifts. *Astrophys. J.* **694**, 1517 (2009).
15. Schreiber, C. *et al.* Jekyll & Hyde: quiescence and extreme obscuration in a pair of massive galaxies 1.5 Gyr after the Big Bang. *Astron. Astrophys.* **611**, A22 (2018).
16. Riguccini, L. *et al.* The composite nature of Dust-Obscured Galaxies (DOGs) at z ∼ 2-3 in the COSMOS field - I. A far-infrared view. *Mon. Not. R. Astron. Soc.* **452**, 470–485 (2015).
17. Bouwens, R. J. *et al.* UV-continuum Slopes at z ˜ 4-7 from the HUDF09+ERS+CANDELS Observations: Discovery of a Well-defined UV Color-Magnitude Relationship for z >= 4 Star-forming Galaxies. *Astrophys. J.* **754**, 83 (2012).
18. Straatman, C. M. S. *et al.* A Substantial Population of Massive Quiescent Galaxies at z ˜ 4 from ZFOURGE. *Astrophys. J. Let.* **783**, L14 (2014).
19. Henriques, B. M. B. *et al.* Galaxy formation in the Planck cosmology - I. Matching the observed evolution of star formation rates, colours and stellar masses. *Mon. Not. R. Astron. Soc.* **451**, 2663–2680 (2015).
20. Snyder, G. F. *et al.* Massive close pairs measure rapid galaxy assembly in mergers at high redshift. *Mon. Not. R. Astron. Soc.* **468**, 207–216 (2017).
21. Steinhardt, C. L., Capak, P., Masters, D. & Speagle, J. S. The Impossibly Early Galaxy Problem. *Astrophys. J.* **824**, 21 (2016).
22. Straatman, C. M. S. *et al.* The FourStar Galaxy Evolution Survey (ZFOURGE): Ultraviolet to Far-infrared Catalogs, Medium-bandwidth Photometric Redshifts with Improved Accuracy, Stellar Masses, and Confirmation of Quiescent Galaxies to z ∼ 3.5. *Astrophys. J.* **830**, 51 (2016).
23. da Cunha, E. *et al.* An ALMA Survey of Sub-millimeter Galaxies in the Extended Chandra Deep Field South: Physical Properties Derived from Ultraviolet-to-radio Modeling. *Astrophys. J.* **806**, 110 (2015).
24. Schreiber, C. *et al.* The Herschel view of the dominant mode of galaxy growth from z = 4 to the present day. *Astron. Astrophys.* **575**, A74 (2015).
25. Ono, Y. *et al.* Great Optically Luminous Dropout Research Using Subaru HSC (GOLDRUSH). I. UV luminosity functions at z ∼ 4-7 derived with the half-million dropouts on the 100 deg^2 sky. *Publ. Astron. Soc. Jpn.* **70**, S10 (2018).
26. Harikane, Y. *et al.* GOLDRUSH. II. Clustering of galaxies at z ∼ 4-6 revealed with the half-million dropouts over the 100 deg^2 area corresponding to 1 Gpc^3. *Publ. Astron. Soc. Jpn.* **70**, S11 (2018).
27. Hartley, W. G. *et al.* Studying the emergence of the red sequence through galaxy clustering: host halo masses at z > 2. *Mon. Not. R. Astron. Soc.* **431**, 3045–3059 (2013).
28. Mo, H. J. & White, S. D. M. The abundance and clustering of dark haloes in the standard ΛCDM cosmogony. *Mon. Not. R. Astron. Soc.* **336**, 112–118 (2002).
29. Fakhouri, O., Ma, C.-P. & Boylan-Kolchin, M. The merger rates and mass assembly histories of dark matter haloes in the two Millennium simulations. *Mon. Not. R. Astron. Soc.* **406**, 2267–2278 (2010).

METHODS

Here we give details of the multi-wavelength observations and the estimation of physical properties of sample galaxies. Throughout we adopt a Chabrier initial mass function[30] and the concordance cosmology with $\Omega_M = 0.3$, $\Omega_\Lambda = 0.7$, and $H_0 = 70$ km s^{-1} Mpc^{-1}. All magnitudes are in the AB system.

1 Observations

1.1 Selection of $H-$dropouts and incompleteness correction We have crossmatched the F160W-selected catalog from the three CANDELS fields (Table 1) with an IRAC 3.6 and 4.5 μm selected catalog[31] from the SEDS survey. The SEDS survey covers the three fields of H-dropouts to a depth of 26 AB mag (3σ) at both 3.6 and 4.5 μm and is 80% complete down to $[4.5] \sim 24$ mag. We first matched sources with $[4.5] < 24$ mag in the SEDS catalog to the F160W-selected catalog and identified those without H-band counterparts within a 2" radius (corresponding roughly to the PSF size of IRAC 3.6 and 4.5 μm). This 4.5 μm magnitude cut was applied to enable sufficient color range to identify extremely red objects while keeping a complete 4.5 μm selected sample. We then visually inspected the IRAC images and excluded sources whose flux is contaminated by bright neighbors as well as those falling on the edge of the F160W image. With knowledge of their positions, some of these H-dropouts are marginally detected in the F160W band but exhibit extended profiles and are unidentifiable as real sources without that prior knowledge. This left us 63 sources with 2 of them serendipitously detected in previous band-7 continuum observations with ALMA.

The criterion of no HST counterparts within 2" radius ensures a clean selection of H-dropouts with reliable constrains of IRAC fluxes. However, given the high density of HST sources in these deep fields, the chance probability of an IRAC-HST coincidence (with distance < 2") is non-negligible . This means that we may have missed some $H-$dropouts simply due to the presence of a random HST source falling within the 2" search radius of the IRAC source. To correct for this effect, we calculate the completeness of this selection approach, which is defined as at a given position the probability of finding zero galaxies in the 2" radius, $p(n = 0) = \exp(-N * \pi * \mathrm{radius}^2)$, with N representing the surface density of HST sources. Averaging over the three CANDELS fields yields $N = 0.05$ arcsec^{-2}, implying $p(n = 0) = 0.53$. This suggests that while our approach yields a clean selection of $H-$dropouts, roughly half of the true $H-$dropouts have been missed simply due to chance superposition of sources, which needs to be corrected. In fact, this completeness correction is consistent with recent findings from a blind ALMA survey, which reveals four H-dropouts (with $[4.5] < 24$) that were not picked up by our approach within an area of 1/3 of the GOODS-South filed[32,33], in comparison to 12 sources selected by our approach in the whole GOODS-South field. Among these four sources, 3 of them have at least one HST counterpart within 2" (with the remaining one absent from our IRAC catalog, which is shallower than the one used in[32]), which is inconsistent with being the right counterpart of the ALMA emission based on the redshift and other physical properties. Albeit with small number statistics, this implies a completeness of our searching approach of $\sim 57\%$, consistent with our estimated value. In addition to this correction, we need to also correct for the incompleteness of the IRAC imaging from the SEDS survey, which ranges from 93% at $[4.5] =22$ to 75% -80% at $[4.5] = 24$ in the three fields. Combining the two corrections, a factor of 2 to 2.4 has been applied to the number density (including also star formation rate and stellar mass density) of H-dropouts depending on their IRAC fluxes.

1.2 Multiwavelength photometry In each field, we gathered mosaics in a large number of bands, including all the images used to build the 3DHST[34] and ZFOURGE[22] catalogs. All our galaxies therefore had rich and deep photometry from the UV to the NIR, reaching typical 5σ depths (AB) of 27 in u to i, 26 in z to H, and 25 in Ks. We provide the full detail of the used mosaics below.

For GOODS-South, we used VLT/VIMOS images in the U and R bands[35], ESO/WFI images in the U, $U38$, B, V, R, I bands from GaBoDS[36], CTIO/MOSAIC image in the z band from MUSYC[37], Subaru images in 15 medium bands from MUSYC[38], *Hubble* images in the F395W, F606W, F775W, F8514W, F850LP, F105W, F125W, F160W bands from GOODS and CANDELS programs[39,40,41], VLT/ISAAC images in the J, H, Ks bands[42], CFHT/WIRCam images in the J and Ks bands from TENIS[43], Magellan/FOURSTAR images in the $J1$, $J2$, $J3$, Hs, Hl, Ks bands from ZFOURGE[22], a VLT/HawK-I image in the Ks band from HUGS[44], and *Spitzer* IRAC images from SEDS[31].

For UDS, we used a CFHT/Megacam image in the u band produced by the 3DHST team[34], Subaru images in the B, V, R, i, z bands[45], *Hubble* images in the F606W, F814W, F125W, F140W, F160W bands from the CANDELS and 3DHST programs[41,46], UKIRT/WFCAM images in the J, H, K bands from UKIDSS[47], Magellan/FOURSTAR images in the $J1$, $J2$, $J3$, Hs, Hl, Ks bands from ZFOURGE[22], VLT/HawK-I images in the Y and Ks bands from HUGS[44], and *Spitzer* IRAC images from SEDS[31] and SpUDS (PI: J. Dunlop).

For COSMOS, we used CFHT/Megacam images in the u and i bands from CFHTLS[48], Subaru images in the B, g, V, r, i, z bands as well as 10 medium bands[49], *Hubble* images in the F606W, F814W, F125W, F140W, F160W bands from the CANDELS and 3DHST programs[41,46], CFHT/WIRCam images in the H and Ks bands[50], Magellan/FOURSTAR images in the $J1$, $J2$, $J3$, Hs, Hl, Ks bands from ZFOURGE[22], VISTA/VIRCAM images in the Y, J, H, Ks from UltraVISTA DR3[51], and *Spitzer* IRAC images from SEDS[31] and S-COSMOS[52].

The photometry was obtained with a procedure very similar to that previously used in deep surveys[22,46], which we summarize here. Fluxes in UV-to-NIR were extracted on re-gridded and PSF-matched images in fixed apertures of 2″ diameter. Because of the broader PSF in Spitzer images, fluxes in the IRAC bands were extracted separately, with a 3" aperture and without PSF matching. The asymmetric IRAC PSF was rotated to match the telescope roll angle for each field. Prior to extracting the fluxes, all the neighboring sources within a 10" radius were subtracted from the images. This was done by identifying the sources from a stacked detection image, and using the HST F160W profile of each source as a model. These models were convolved by the PSF of each image, where they were fit simultaneously using a linear solver. Most often the dropouts were not found in the stacked detection image, and were therefore modeled as point-sources at the coordinates of their IRAC centroid during the de-blending stage. Once the flux was extracted, additional "sky" apertures were placed randomly around each dropout. The median flux in these sky apertures was subtracted from the dropout's flux, to eliminate any remaining background signal, while the standard deviation of these fluxes was used as flux uncertainty. Lastly, fluxes and uncertainties were aperture-corrected using the matched PSF's light curve, assuming point-like morphology.

1.3 ALMA observation and data reduction Our ALMA band-7 continuum observations of H-dropouts are performed during January and July 2016. The observations were centered on the IRAC positions with a spectral setup placed around a central frequency of 343.5 GHz. While we asked 0.7″-resolution observation for all the three fields, only the CANDLES-COSMOS field was observed as requested, yielding a synthesis beam of $0.6 \times 1''$. The other two fields were observed at 0.2-0.3″ resolution. The integration time is roughly 1.8 mins per object with a total observing time of ~2 h. We reduced the data using the CASA pipeline (version 4.3.1). To reach an homogeneous angular resolution, we tapered the baselines for these two fields to an angular resolution of 0.6″. This resolution corresponds to ~ 4 kpc at $z = 4$, compared to typical sizes of ~2 kpc for SMGs[53].

We measured the total flux of all our targets directly in the (u, v) plane using the uvmodelfit procedure from the CASA pipeline. The sources were modeled with a circular Gaussian profile of variable total flux, centroid, width, axis ratio and position angle. 39 H-dropouts are detected at S/N> 4 with $S_{870\mu m} > 0.6$ mJy, including two galaxies that were serendipitously detected in a previous ALMA program[54] targeting H-detected $z \sim 4$ galaxies, which has reached similar depth as this observation. The positions of the 870 μm emission as measured from ALMA are in good agreement with IRAC, with ΔRA=0.081±0.128″ and ΔDEC= -0.13±0.16″.

1.4 SCUBA-2 450 μm and VLA observations One of the three H-dropout fields, CANDELS-COSMOS, is covered by deep SCUBA-2 450 μm and 870 μm observations from the STUDIES survey[55]. Previous observations with JCMT/SCUBA-2 at the same region[56,57,58] have also been combined to produce an extremely deep 450 μm image and a confusion-limited 850 μm image. The instrumental noises at 450 μm and 850 μm at the deepest regions reach ~0.65 mJy and ~ 0.1 mJy, respectively.

The SCUBA2-450 μm and -850 μm fluxes for H-dropouts are measured at the position of the IRAC 3.6 and 4.5 μm emission with the prior-based PSF-fitting code FASTPHOT[59]. We further restrict all the extracted fluxes to be positive with bounded value least-square minimization. During the fit we have included all the MIPS 24 μm- and VLA detections as priors to perform source extraction. The VLA 3 GHz observation in COSMOS[60] reaches a rms of 2.3 μJy/beam at an angular resolution of 0.75″, which is deep enough to put useful constraints on their redshifts. The flux measurement for H-dropouts in the far-IR suffers minimum source confusion due to our selection criterion (no close neighbours within a 2″ radius). A comparison of 870 μm fluxes measured by ALMA and SCUBA-2 yields excellent agreement with a median value of $S_{\rm ALMA}/S_{\rm SCUBA-2} = 1.05$.

1.5 X-SHOOTER spectra In the COSMOS field, deep medium band images in the optical were obtained with the Subaru telescope[49]. We visually inspected these images at the location of each dropout in our sample and found three galaxies with flux excesses in one of these images, with a significance above 4 sigma. Examples are shown on Extended Data Figure 6. Such flux excess can be interpreted as coming from a bright emission line[61]. For these three dropouts, the line could be identified as Lyα at $z = 5.0$, 3.2 and 4.1, respectively. Even though H-dropouts are typically very obscured, Lyα may still be detected through un-obscured sight lines, or by scattering[62]. Judging from the spatial offsets of about 1″ we observed between this optical flux excess and the *Spitzer*–IRAC or ALMA emission, scattering appears to be the most plausible explanation.

We thus followed up these objects with VLT/X-SHOOTER to confirm the presence of an emission line. Each dropout was observed in May 2018 in the UVB and VIS arms for 50 minutes in stare mode (no nodding), split in three exposures. The 2D spectra were reduced using the standard pipeline, and 1D spectra were produced by fitting a Gaussian profile to each spectral slice. Uncertainties were controlled by computing the standard deviation of spectral elements in regions without sky lines; we found that the 1D uncertainty spectrum had to be rescaled upwards by a factor 1.27 to match the observed noise.

We then searched for emission lines in the spectra, considering only the wavelength range covered by the Subaru medium band in which the flux excess was previously identified. The result of this search is displayed on Extended Data Figure 6. We found a 10σ detection at 0.498μm for the dropout 32932, corresponding to $z_{\rm spec} = 3.0971 \pm 0.0002$, and a more marginal but still significant 4.3σ detection at 0.739μm for the dropout 25363, corresponding to $z_{\rm spec} = 5.113^{+0.001}_{-0.005}$. Because our search space is tightly limited by the Subaru passband, the latter only has a 0.4% chance of being spurious, and we therefore consider it a reliable detection. The third dropout showed no significant line emission above 2σ.

1.6 Lyman-break galaxy selection In order to compare the properties of $H-$dropouts and LBGs[63], we have selected LBGs using the ZFOURGE catalogs in the same three CANDELS fields[22]. The advantage of the ZFOURGE catalog is that it is essentially a K_s-band selected catalog, for which the deep K_s band data provides critical constraints on the redshift and stellar masses estimates at $z > 4$. We select our $z = 4 - 6$ LBG galaxy sample using the selection criterion in[64]. Due to the lack of B-band data from HST, the $z \sim 4$ LBG sample is only limited to GOODS-South field while the $z \sim 5$ and $z \sim 6$ LBG sample include galaxies from all the three fields. To enable a clean selection of galaxies with reliable flux density measurements, we have further limited the selection to galaxies with $use = 1$ as recommended[22]. This reduces the effective area to 132.2, 139.2, and 135.6 arcmin^2 for GOODS-South, COSMOS, and UDS, respectively. To identify total SFRD from massive LBGs with $M_* > 10^{10.3} M_\odot$, we utilized the latest determination of the UV luminosity function at $z \sim 4 - 6$[25]. Taking into account variations in the $M_* - M_{UV}$ relation, this mass cut corresponds to $M_{UV} < [-21.55, -22.04, -22.27]$ at $z = [4, 5, 6]$, respectively. We then derive the dust-corrected SFR for these brightest UV-selected galaxies following the approach in ref. [17].

2 Determination of Physical Properties

2.1 Stacked UV-to-NIR SEDs To produce the stacked UV-to-NIR SEDs, we took the fluxes of each galaxy in our photometric catalog and normalized them by their respective IRAC 4.5 μm flux. We then computed the mean flux in each band, using inverse variance weighting, and finally multiplied the resulting stacked fluxes by the average 4.5 μm flux of the stacked sample. In the stack, we combined bands that have similar effective wavelengths, even though the true passbands could be slightly different; for example we stacked together all the *K*s bands from UKIDSS, UltraVISTA, FOURSTAR, WIRCam, and ISAAC into a single *K*s band. The uncertainties on the stacked fluxes were derived by formally combining the uncertainties of each stacked galaxy. We note that, since we obtained our photometry using fixed-size apertures, this method is strictly equivalent to stacking the images.

2.2 Photometric redshift and stellar mass determination Using the aforementioned multiwavelength photometry, including bands with formal non-detections, photometric redshifts were computed with EAzY[65] using the full set of template SEDs, namely, including the old-and-dusty template and the extreme emission line template. The prior on the observed magnitudes was not used. Using these redshifts, we then ran FAST[66] to estimate the stellar masses. We assumed a delayed-exponentially-declining star-formation history, with a range of age and exponential timescale. Dust attenuation was modeled with the[67] prescription, allowing A_V up to 6 magnitudes. Metallicity was fixed to solar during the fitting. We also used the infrared luminosities inferred from the ALMA fluxes to further constrain the fits. This was implemented as follows. From the stacked Herschel SED (see Figure 3), we measured the mean dust temperature of our sample: $T_{\rm dust} = 36.7 \pm 2.1$ K. Based on Herschel and ALMA observations of $z > 2$ galaxies[13], we expect a typical scatter of 5 K around the average temperature at any given redshift. Assuming this distribution of temperatures holds for the dropouts, we generated probability distributions for $L_{\rm IR}$ using a Monte Carlo procedure: the measured ALMA flux was randomly perturbed with Gaussian noise of amplitude set by the flux uncertainty, and the dust temperature was drawn from a Gaussian distribution centered on 36.7 K and with a width of 5 K; the resulting dust SED was then used to extrapolate $L_{\rm IR}$ from the ALMA measurement. For galaxies whose ALMA flux has $S/N < 2$, the resulting probability distribution of $L_{\rm IR}$ was close to Gaussian, while for the detections the probability distribution was close to log-normal. We modeled these two regimes accordingly in the fit, by assuming either Gaussian noise on $L_{\rm IR}$ or $\log_{10}(L_{\rm IR})$, respectively. The observed infrared luminosity was then compared to the modeled value, which we computed as the difference of bolometric luminosity before after applying dust attenuation. This resulted in an additional contribution to the χ^2, which was then used for standard model selection.

Uncertainties on the photometric redshifts were derived from the 16th and 84th percentiles of the probability distribution produced by EAzY. This accounts for uncertainty in the photometry as well as on the model galaxy templates. Uncertainties on the derived physical parameters, including the stellar mass, were derived using Monte Carlo simulations, where the observed photometry was randomly perturbed with Gaussian noise of amplitude determined by the estimated photometric uncertainties. This was repeated 200 times. The error bars on physical parameters were then derived from the 16th and 84th percentiles of the distribution of the values obtained in the Monte Carlo simulations. For each fit, the redshift was left free to vary within the 68% confidence interval reported by the photometric redshift code. Therefore the resulting error bars account for uncertainties on the photometry and on the redshift.

2.3 Clustering measurements Since the number of H-dropouts is small, we calculate two-point angular cross-correlation function (CCF) with a much larger population of galaxies sharing the same cosmic volume (redshifts) in order to enhance the statistics. Specifically we select all the galaxies with $3.5 < z < 5.5$ from the *H*-selected catalog in the same three CANDELS fields (“the galaxy sample”, hereafter), and then calculate CCF using the estimator as follows[68]:

$$\omega(\theta) = \frac{HG(\theta) - HR(\theta) - GR(\theta) + RR(\theta)}{RR(\theta)} \qquad (1)$$

where HG, HR, GR, RR are Hdropout-galaxy, Hdropout-random, galaxy-random and random-random pair counts respectively. The random galaxy sample are created within the same CANDELS footprint as the H-dropouts (we exclude HUDF in the GOODS-S field because of its much deeper integration than other regions). The uncertainties of CCF are estimated as:

$$\Delta\omega(\theta) = \frac{1+\omega(\theta)}{\sqrt{HG(\theta)}}. \tag{2}$$

We then fit the derived CCF with a power-law model:

$$\omega(\theta) = A_\omega \theta^{-\beta} - IC, \tag{3}$$

where A_ω is the correlation amplitude and β is the power-law index fixed to 0.8 and IC is the integral constraint. Integral constraints is an offset due to the clustering measurement over the limited area and is calculated by

$$IC = \frac{\sum RR(\theta) A_\omega \theta^{-\beta}}{\sum RR(\theta)}. \tag{4}$$

The derived correlation amplitude can be converted to three-dimensional correlation length r_0 by Limber equation[69] modified by[70] for the cross-correlation.

The correlation length is related to galaxy bias b, such that

$$\sigma^2_{8,\mathrm{gal}} = \frac{72}{(3-\gamma)(4-\gamma)(6-\gamma)2^\gamma}\left(\frac{r_0}{8\,h^{-1}\mathrm{Mpc}}\right)^\gamma \tag{5}$$

and

$$b = \frac{\sigma_{8,\mathrm{gal}}}{\sigma_8(z)}, \tag{6}$$

where $\sigma_{8,\mathrm{gal}}$ is a galaxy fluctuation, $\gamma = 1+\beta$, and $\sigma_8(z)$ is a matter fluctuation[71]. The halo mass is then derived from the estimated galaxy bias[28].

30. Chabrier, G. Galactic Stellar and Substellar Initial Mass Function. *Publ. Astron. Soc. Pac.* **115**, 763–795 (2003). `arXiv:astro-ph/0304382`.

31. Ashby, M. L. N. *et al.* SEDS: The Spitzer Extended Deep Survey. Survey Design, Photometry, and Deep IRAC Source Counts. *Astrophys. J.* **769**, 80 (2013).

32. Franco, M. *et al.* GOODS-ALMA: 1.1 mm galaxy survey. I. Source catalog and optically dark galaxies. *Astron. Astrophys.* **620**, A152 (2018). `1803.00157`.

33. Yamaguchi, Y. *et al.* ALMA twenty-six arcmin$2̂$ survey of GOODS-S at one-millimeter (ASAGAO): Near-infrared-dark faint ALMA sources. *arXiv e-prints* arXiv:1903.02744 (2019). `1903.02744`.

34. Skelton, R. E. *et al.* 3D-HST WFC3-selected Photometric Catalogs in the Five CANDELS/3D-HST Fields: Photometry, Photometric Redshifts, and Stellar Masses. *Astrophys. J. Supp.* **214**, 24 (2014). `1403.3689`.

35. Nonino, M. *et al.* Deep U Band and R Imaging of Goods-South: Observations, Data Reduction and First Results. *Astrophys. J. Supp.* **183**, 244–260 (2009). `0906.4250`.

36. Hildebrandt, H. *et al.* GaBoDS: The Garching-Bonn Deep Survey. V. Data release of the ESO Deep-Public-Survey. *Astron. Astrophys.* **452**, 1121–1128 (2006). `astro-ph/0509882`.

37. Gawiser, E. *et al.* The Multiwavelength Survey by Yale-Chile (MUSYC): Survey Design and Deep Public UBVRIz' Images and Catalogs of the Extended Hubble Deep Field-South. *Astrophys. J. Supp.* **162**, 1–19 (2006). `astro-ph/0509202`.

38. Cardamone, C. N. *et al.* The Multiwavelength Survey by Yale-Chile (MUSYC): Deep Medium-band Optical Imaging and High-quality 32-band Photometric Redshifts in the ECDF-S. *Astrophys. J. Supp.* **189**, 270–285 (2010).

39. Giavalisco, M. *et al.* The Great Observatories Origins Deep Survey: Initial Results from Optical and Near-Infrared Imaging. *Astrophys. J. Let.* **600**, L93–L98 (2004). `arXiv:astro-ph/0309105`.

40. Grogin, Norman A. *et al.* CANDELS: The Cosmic Assembly Near-infrared Deep Extragalactic Legacy Survey. *Astrophys. J. Supp.* **197**, 35 (2011). `1105.3753`.

41. Koekemoer, A. M. *et al.* CANDELS: The Cosmic Assembly Near-infrared Deep Extragalactic Legacy Survey - The Hubble Space Telescope Observations, Imaging Data Products, and Mosaics. *Astrophys. J. Supp.* **197**, 36 (2011). `1105.3754`.

42. Retzlaff, J. *et al.* The Great Observatories Origins Deep Survey. VLT/ISAAC near-infrared imaging of the GOODS-South field. *Astron. Astrophys.* **511**, 50 (2010). `0912.1306`.

43. Hsieh, B.-C. *et al.* The Taiwan ECDFS Near-Infrared Survey: Ultra-deep J and K_S Imaging in the Extended Chandra Deep Field-South. *Astrophys. J. Supp.* **203**, 23 (2012). `1210.4519`.

44. Fontana, A. *et al.* The Hawk-I UDS and GOODS Survey (HUGS): Survey design and deep K-band number counts. *Astron. Astrophys.* **570**, A11 (2014). `1409.7082`.

45. Furusawa, H. *et al.* The Subaru/XMM-Newton Deep Survey (SXDS). II. Optical Imaging and Photometric Catalogs. *Astrophys. J. Supp.* **176**, 1–18 (2008). `0801.4017`.

46. Momcheva, I. G. *et al.* The 3D-HST Survey: Hubble Space Telescope WFC3/G141 Grism Spectra, Redshifts, and Emission Line Measurements for ˜ 100,000 Galaxies. *Astrophys. J. Supp.* **225**, 27 (2016). `1510.02106`.

47. Lawrence, A. *et al.* The UKIRT Infrared Deep Sky Survey (UKIDSS). *Mon. Not. R. Astron. Soc.* **379**, 1599–1617 (2007). `arXiv:astro-ph/0604426`.

48. Cuillandre, J.-C. J. *et al.* Introduction to the CFHT Legacy Survey final release (CFHTLS T0007). In *Observatory Operations: Strategies, Processes, and Systems IV,* vol. 8448 of *Proc. SPIE,* 84480M (2012).

49. Taniguchi, Y. *et al.* The Cosmic Evolution Survey (COSMOS): Subaru Observations of the HST Cosmos Field. *The Astrophysical Journal Supplement Series* **172**, 9–28 (2007).

50. McCracken, H. J. *et al.* The COSMOS-WIRCam Near-Infrared Imaging Survey. I. BzK-Selected Passive and Star-Forming Galaxy Candidates at z gsim 1.4. *Astrophys. J.* **708**, 202–217 (2010). `0910.2705`.

51. McCracken, H. J. *et al.* UltraVISTA: a new ultra-deep near-infrared survey in COSMOS. *Astron. Astrophys.* **544**, A156 (2012). `1204.6586`.

52. Sanders, D. B. *et al.* S-COSMOS: The Spitzer Legacy Survey of the Hubble Space Telescope ACS 2 deg^2 COSMOS Field I: Survey Strategy and First Analysis. *Astrophys. J. Supp.* **172**, 86–98 (2007). `arXiv:astro-ph/0701318`.

53. Hodge, J. A. *et al.* Kiloparsec-scale Dust Disks in High-redshift Luminous Submillimeter Galaxies. *Astrophys. J.* **833**, 103 (2016). `1609.09649`.

54. Schreiber, C. *et al.* Observational evidence of a slow downfall of star formation efficiency in massive galaxies during the past 10 Gyr. *Astron. Astrophys.* **589**, A35 (2016). `1601.04226`.

55. Wang, W.-H. *et al.* SCUBA-2 Ultra Deep Imaging EAO Survey (STUDIES): Faint-end Counts at 450 μm. *Astrophys. J.* **850**, 37 (2017). `1707.00990`.

56. Casey, C. M. *et al.* Characterization of SCUBA-2 450 μm and 850 μm selected galaxies in the COSMOS field. *Mon. Not. R. Astron. Soc.* **436**, 1919–1954 (2013). `1302.2619`.

57. Geach, J. E. *et al.* The SCUBA-2 Cosmology Legacy Survey: blank-field number counts of 450-μm-selected galaxies and their contribution to the cosmic infrared background. *Mon. Not. R. Astron. Soc.* **432**, 53–61 (2013). `1211.6668`.

58. Geach, J. E. *et al.* The SCUBA-2 Cosmology Legacy Survey: 850 μm maps, catalogues and number counts. *Mon. Not. R. Astron. Soc.* **465**, 1789–1806 (2017). `1607.03904`.

59. Béthermin, M., Dole, H., Cousin, M. & Bavouzet, N. Submillimeter number counts at 250 μm, 350 μm and 500 μm in BLAST data. *Astron. Astrophys.* **516**, A43 (2010). `1003.0833`.

60. Smolčić, V. *et al.* The VLA-COSMOS 3 GHz Large Project: Continuum data and source catalog release. *Astron. Astrophys.* **602**, A1 (2017). `1703.09713`.

61. Sobral, D. *et al.* Slicing COSMOS with SC4K: the evolution of typical Ly α emitters and the Ly α escape fraction from z? 2 to 6. *Mon. Not. R. Astron. Soc.* **476**, 4725–4752 (2018).

62. Finkelstein, S. L., Rhoads, J. E., Malhotra, S., Grogin, N. & Wang, J. Effects of Dust Geometry in Lyα Galaxies at z = 4.4. *Astrophys. J.* **678**, 655–668 (2008).

63. Steidel, C. C., Giavalisco, M., Pettini, M., Dickinson, M. & Adelberger, K. L. Spectroscopic Confirmation of a Population of Normal Star-forming Galaxies at Redshifts Z > 3. *Astrophys. J. Let.* **462**, L17 (1996). `astro-ph/9602024`.

64. Bouwens, R. J. *et al.* UV Luminosity Functions at Redshifts z? 4 to z? 10: 10,000 Galaxies from HST Legacy Fields. *Astrophys. J.* **803**, 34 (2015). `1403.4295`.

65. Brammer, G. B., van Dokkum, P. G. & Coppi, P. EAZY: A Fast, Public Photometric Redshift Code. *Astrophys. J.* **686**, 1503–1513 (2008). `0807.1533`.

66. Kriek, M. *et al.* An Ultra-Deep Near-Infrared Spectrum of a Compact Quiescent Galaxy at z = 2.2. *Astrophys. J.* **700**, 221–231 (2009). `0905.1692`.

67. Calzetti, D. The Dust Opacity of Star-forming Galaxies. *Publ. Astron. Soc. Pac.* **113**, 1449–1485 (2001). `astro-ph/0109035`.

68. Landy, S. D. & Szalay, A. S. Bias and variance of angular correlation functions. *Astrophys. J.* **412**, 64–71 (1993).

69. Limber, D. N. The Analysis of Counts of the Extragalactic Nebulae in Terms of a Fluctuating Density Field. *Astrophys. J.* **117**, 134 (1953).

70. Croom, S. M. & Shanks, T. Radio-quiet QSO environments - I. The correlation of QSOs and b_J<23 galaxies. *Mon. Not. R. Astron. Soc.* **303**, 411–422 (1999). `astro-ph/9810170`.

71. Peebles, P. J. E. *Principles of Physical Cosmology* (Princeton University Press, 1993).

72. Combes, F. *et al.* A bright z = 5.2 lensed submillimeter galaxy in the field of Abell 773. HLSJ091828.6+514223. *Astron. Astrophys.* **538**, L4 (2012).

73. Vieira, J. D. *et al.* Dusty starburst galaxies in the early Universe as revealed by gravitational lensing. *Nature* **495**, 344–347 (2013). `1303.2723`.

74. Carilli, C. L. & Yun, M. S. The Radio-to-Submillimeter Spectral Index as a Redshift Indicator. *Astrophys. J. Let.* **513**, L13–L16 (1999). `astro-ph/9812251`.

75. Boquien, M. *et al.* CIGALE: a python Code Investigating GALaxy Emission. *Astron. Astrophys.* **622**, A103 (2019). `1811.03094`.

76. Bruzual, G. & Charlot, S. Stellar population synthesis at the resolution of 2003. *Mon. Not. R. Astron. Soc.* **344**, 1000–1028 (2003). `arXiv:astro-ph/0309134`.

77. Draine, B. T. & Li, A. Infrared Emission from Interstellar Dust. IV. The Silicate-Graphite-PAH Model in the Post-Spitzer Era. *Astrophys. J.* **657**, 810–837 (2007). `astro-ph/0608003`.

78. Inoue, A. K. Rest-frame ultraviolet-to-optical spectral characteristics of extremely metal-poor and metal-free galaxies. *Mon. Not. R. Astron. Soc.* **415**, 2920–2931 (2011). `1102.5150`.

EXTENDED DATA

Extended Data Table. 1 | Survey depths for each field

Field	Area arcmin^2	WFC3/F160W (5σ)	H-dropouts ([4.5] < 24)	ALMA-detected ($S_{870\mu m} > 0.6$ mJy)	ALMA-undetected ($S_{870\mu m} < 0.6$ mJy)
CANDELS-GDS	184	$H < 27.4$–29.7	12	10	2
CANDELS-UDS	202	$H < 27.1$–27.6	33	14	19
CANDELS-COSMOS	208	$H < 27.4$–27.8	18	15	3

Extended Data Table. 2 | Physical properties of H-dropouts

ID	R.A. (J2000)	Decl. (J2000)	[4.5]	$S_{870\mu m}$ (mJy)	z	Log M_* $M_\odot$
GDS-25526	03:32:47.97	-27:54:16.4	22.05	8.34±0.18	$4.74^{+0.28}_{-0.30}$	$10.84^{+0.05}_{-0.17}$
GDS-27571	03:32:30.62	-27:42:24.3	22.44	0.82±0.16	$4.64^{+0.19}_{-1.64}$	$10.89^{+0.04}_{-0.48}$
GDS-40613	03:32:11.44	-27:52:07.1	23.17	1.83±0.18	$3.04^{+0.22}_{-0.35}$	$10.64^{+0.02}_{-0.22}$
GDS-43215	03:32:20.34	-27:42:28.8	23.02	1.52±0.16	$2.91^{+0.19}_{-0.22}$	$10.25^{+0.03}_{-0.53}$
GDS-44539	03:32:28.59	-27:48:50.2	23.41	0.69±0.10	$4.22^{+0.77}_{-0.67}$	$10.94^{+0.03}_{-0.31}$
GDS-47375	03:32:14.62	-27:43:06.0	23.48	1.89±0.12	$3.60^{+0.66}_{-0.66}$	$10.27^{+0.13}_{-0.12}$
GDS-48764	03:32:32.31	-27:54:26.9	23.31	2.54±0.42	$5.16^{+3.08}_{-1.73}$	$10.38^{+0.51}_{-0.03}$
GDS-48885	03:32:47.17	-27:45:25.1	23.57	0.87±0.11	$4.62^{+0.19}_{-0.17}$	$10.56^{+0.02}_{-0.08}$
GDS-49094	03:32:31.85	-27:43:12.7	23.59	0.89±0.13	$3.69^{+0.29}_{-0.28}$	$10.29^{+0.10}_{-0.05}$
GDS-52734	03:32:10.10	-27:50:33.1	24.06	1.41±0.15	$5.13^{+1.72}_{-1.18}$	$10.71^{+0.17}_{-0.21}$
GDS-54513	03:32:04.99	-27:41:56.5	23.71	<0.6	$4.33^{+0.32}_{-0.37}$	$10.30^{+0.00}_{-0.37}$
GDS-58560	03:32:40.11	-27:42:55.3	23.85	<0.6	$5.35^{+2.33}_{-2.18}$	$10.58^{+0.39}_{-0.43}$
COS-16199	10:00:25.41	+02:25:43.9	21.96	3.91±0.09	$6.54^{+1.43}_{-1.54}$	$10.90^{+0.14}_{-0.27}$
COS-19762	10:00:15.89	+02:24:45.9	22.94	4.35±0.10	$3.52^{+5.36}_{-0.19}$	$10.79^{+0.88}_{-0.08}$
COS-23718	10:00:28.95	+02:25:05.3	22.82	2.25±0.10	$5.77^{+0.80}_{-0.88}$	$11.02^{+0.13}_{-0.24}$
COS-23913	10:00:23.03	+02:21:55.0	22.87	1.63±0.09	$3.65^{+0.35}_{-0.29}$	$10.65^{+0.10}_{-0.11}$
COS-24466	10:00:38.07	+02:28:06.2	23.22	1.38±0.09	$3.35^{+0.39}_{-0.38}$	$10.37^{+0.34}_{-0.26}$
COS-25270	10:00:23.62	+02:13:57.4	23.47	<0.6	$3.78^{+0.55}_{-0.56}$	$10.48^{+0.04}_{-0.20}$
COS-25363	10:00:26.68	+02:31:26.2	23.15	3.0 ±0.2	$5.113^{+0.001}_{-0.005}$	$10.52^{+0.09}_{-0.19}$
COS-25881	10:00:27.03	+02:24:24.0	22.96	1.30±0.10	$6.58^{+1.43}_{-1.38}$	$11.12^{+0.17}_{-0.30}$
COS-27285	10:00:27.79	+02:25:52.2	23.74	1.58±0.09	$4.32^{+0.23}_{-0.22}$	$10.31^{+0.14}_{-0.06}$
COS-27392	10:00:27.98	+02:25:29.7	23.42	<0.6	$3.61^{+0.51}_{-0.49}$	$10.38^{+0.11}_{-0.08}$
COS-30182	10:00:14.70	+02:28:01.7	23.08	1.59±0.09	$6.37^{+1.16}_{-2.15}$	$10.94^{+0.22}_{-0.28}$
COS-30614	10:00:14.69	+02:30:04.6	23.39	0.85±0.10	$3.97^{+0.19}_{-0.29}$	$10.22^{+0.04}_{-0.14}$
COS-31278	10:00:26.09	+02:12:31.6	23.36	0.93±0.09	$3.37^{+0.43}_{-0.35}$	$10.14^{+0.13}_{-0.15}$
COS-31483	10:00:46.50	+02:23:09.1	23.89	0.70±0.11	$2.97^{+0.40}_{-0.41}$	$9.91^{+0.13}_{-0.13}$
COS-31661	10:00:41.83	+02:25:47.0	23.28	2.88±0.12	$3.72^{+0.17}_{-0.19}$	$10.36^{+0.05}_{-0.20}$
COS-32409	10:00:15.84	+02:23:04.0	23.66	0.70±0.11	$3.91^{+1.66}_{-1.16}$	$9.87^{+0.48}_{-0.06}$
COS-32932	10:00:22.44	+02:23:41.1	23.22	<0.6	$3.0971^{+0.0002}_{-0.001}$	$9.96^{+0.15}_{-0.11}$
COS-34487	10:00:35.34	+02:28:26.7	23.36	4.3 ±0.15	$3.15^{+0.52}_{-0.60}$	$10.18^{+0.26}_{-0.20}$
UDS-24945	02:16:59.77	-05:11:52.8	22.16	<0.6	$3.50^{+0.76}_{-0.61}$	$10.76^{+0.22}_{-0.11}$
UDS-29006	02:17:05.52	-05:08:45.8	22.71	<0.6	$3.79^{+0.54}_{-0.53}$	$10.46^{+0.12}_{-0.21}$
UDS-31037	02:18:07.67	-05:13:26.8	22.58	1.83±0.13	$3.62^{+0.70}_{-0.65}$	$10.49^{+0.26}_{-0.07}$
UDS-31072	02:17:43.32	-05:11:57.4	22.29	3.63±0.25	$4.20^{+4.17}_{-0.44}$	$11.31^{+0.33}_{-0.09}$
UDS-31959	02:18:11.36	-05:16:23.7	22.98	<0.6	$3.88^{+0.68}_{-0.73}$	$10.22^{+0.19}_{-0.14}$
UDS-34637	02:18:05.80	-05:11:23.1	22.89	1.07±0.37	$2.84^{+0.54}_{-0.44}$	$10.33^{+0.16}_{-0.17}$
UDS-37344	02:18:02.86	-05:15:05.4	23.36	<0.6	$2.89^{+1.43}_{-1.48}$	$10.18^{+0.08}_{-0.63}$
UDS-37423	02:18:10.02	-05:11:31.5	23.07	1.12±0.15	$7.47^{+0.63}_{-0.64}$	$11.17^{+0.20}_{-0.08}$
UDS-37560	02:17:03.44	-05:15:51.3	22.72	4.40±0.14	$3.95^{+0.35}_{-0.34}$	$10.35^{+0.22}_{-0.17}$
UDS-37649	02:17:36.95	-05:16:07.3	23.14	1.25±0.31	$2.82^{+0.44}_{-0.48}$	$10.31^{+0.11}_{-0.07}$
UDS-40772	02:17:36.56	-05:12:52.0	23.19	1.96±0.31	$4.00^{+0.98}_{-0.98}$	$10.87^{+0.00}_{-0.40}$
UDS-41502	02:17:18.03	-05:11:03.9	23.23	1.59±0.20	$3.73^{+0.44}_{-0.43}$	$10.59^{+0.09}_{-0.33}$
UDS-41525	02:16:59.59	-05:14:15.4	23.34	<0.6	$6.13^{+1.08}_{-1.01}$	$11.17^{+0.15}_{-0.16}$
UDS-41773	02:18:07.02	-05:09:18.1	23.11	1.54±0.15	$3.52^{+1.35}_{-0.84}$	$10.20^{+0.56}_{-0.24}$
UDS-42280	02:18:11.16	-05:10:27.1	23.88	1.16±0.37	$4.21^{+0.18}_{-0.17}$	$10.06^{+0.09}_{-0.16}$
UDS-42875	02:18:21.15	-05:09:42.5	23.04	1.74±0.15	$7.20^{+1.20}_{-1.83}$	$11.75^{+0.05}_{-0.34}$
UDS-43941	02:17:43.65	-05:14:23.9	23.46	1.91±0.11	$3.39^{+0.23}_{-0.23}$	$10.17^{+0.02}_{-0.10}$
UDS-44515	02:18:20.89	-05:11:11.1	23.48	<0.6	$4.20^{+1.35}_{-1.35}$	$10.59^{+0.07}_{-0.27}$
UDS-44594	02:17:20.20	-05:11:55.4	23.79	0.66±0.14	$4.44^{+0.52}_{-0.39}$	$10.60^{+0.04}_{-0.17}$
UDS-45868	02:18:15.00	-05:10:02.7	23.61	<0.6	$3.66^{+0.88}_{-0.88}$	$10.45^{+0.13}_{-0.13}$
UDS-46241	02:17:58.31	-05:15:00.3	23.44	<0.6	$2.18^{+0.78}_{-0.53}$	$9.72^{+0.22}_{-0.38}$
UDS-46513	02:18:17.87	-05:11:53.9	23.84	0.58±0.11	$3.54^{+0.95}_{-0.93}$	$10.31^{+0.11}_{-0.19}$
UDS-46648	02:17:08.17	-05:15:37.8	23.52	2.27±0.20	$6.88^{+1.67}_{-1.74}$	$11.37^{+0.30}_{-0.43}$
UDS-46693	02:17:59.07	-05:09:37.5	23.47	<0.6	$3.56^{+0.37}_{-0.26}$	$10.24^{+0.05}_{-0.29}$
UDS-48514	02:17:29.83	-05:14:23.5	23.65	<0.6	$2.59^{+0.93}_{-0.83}$	$10.04^{+0.03}_{-0.42}$
UDS-49119	02:17:07.14	-05:12:54.0	23.77	1.34±0.30	$4.60^{+1.94}_{-1.83}$	$10.65^{+0.01}_{-0.53}$
UDS-49199	02:18:21.40	-05:11:46.3	23.6	<0.6	$3.96^{+0.84}_{-0.97}$	$10.66^{+0.04}_{-0.24}$
UDS-49594	02:18:01.13	-05:13:45.7	23.65	<0.6	$3.77^{+0.48}_{-0.55}$	$9.79^{+0.03}_{-0.26}$
UDS-49784	02:17:37.48	-05:09:47.7	23.6	<0.6	$3.95^{+1.63}_{-2.21}$	$9.91^{+0.41}_{-0.77}$
UDS-51119	02:17:58.29	-05:11:44.7	23.75	<0.6	$3.45^{+1.16}_{-1.16}$	$10.25^{+0.12}_{-0.13}$
UDS-52324	02:17:06.27	-05:09:48.3	23.49	2.69±0.16	$4.95^{+1.74}_{-1.61}$	$10.62^{+0.12}_{-0.26}$
UDS-54074	02:17:09.70	-05:15:11.3	23.75	0.81±0.10	$5.89^{+1.90}_{-2.37}$	$10.65^{+0.17}_{-0.35}$
UDS-63094	02:17:53.06	-05:11:25.5	23.98	<0.6	$5.08^{+0.24}_{-0.26}$	$10.00^{+0.08}_{-0.27}$

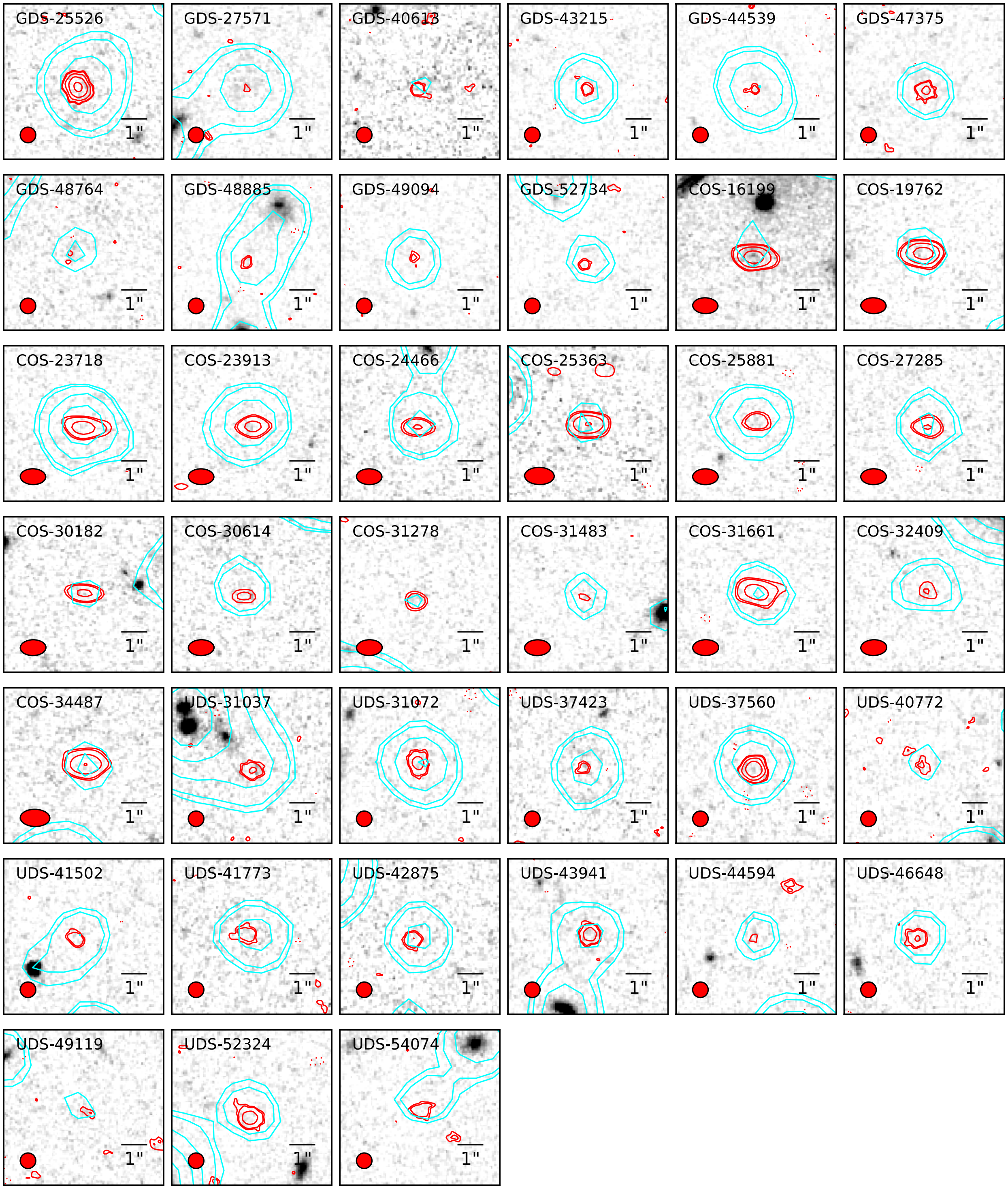

Extended Data Fig. 1 | NIR and ALMA submillimeter-wavelength images of the ALMA-detected H-dropouts. Images are $6'' \times 6''$, centered at the centroid of the IRAC 4.5 μm emission. The greyscale images are F160W-band (*H*-band) exposures from the Hubble Space Telescope Wide Field Camera 3 (HST/WFC3). The red solid contours are ALMA 870 μm imaging, with contour levels starting at 3σ and increasing as 4σ, 8σ, 16σ, 32σ, and 64σ. Negative contours at the same significances are shown with red dashed lines. The cyan contours are 4.5-μm emission, starting at 2σ and increasing as 3σ, 4σ, 8σ and 16σ. The exposure times for HST/WFC3 and ALMA imaging are roughly 2 h and 2 min per object, respectively. Although these H-dropouts are not detected in the deep F160W imaging ($\mathrm{mag}_H \gtrsim 27$), they are significantly detected with ALMA within a short integration time.

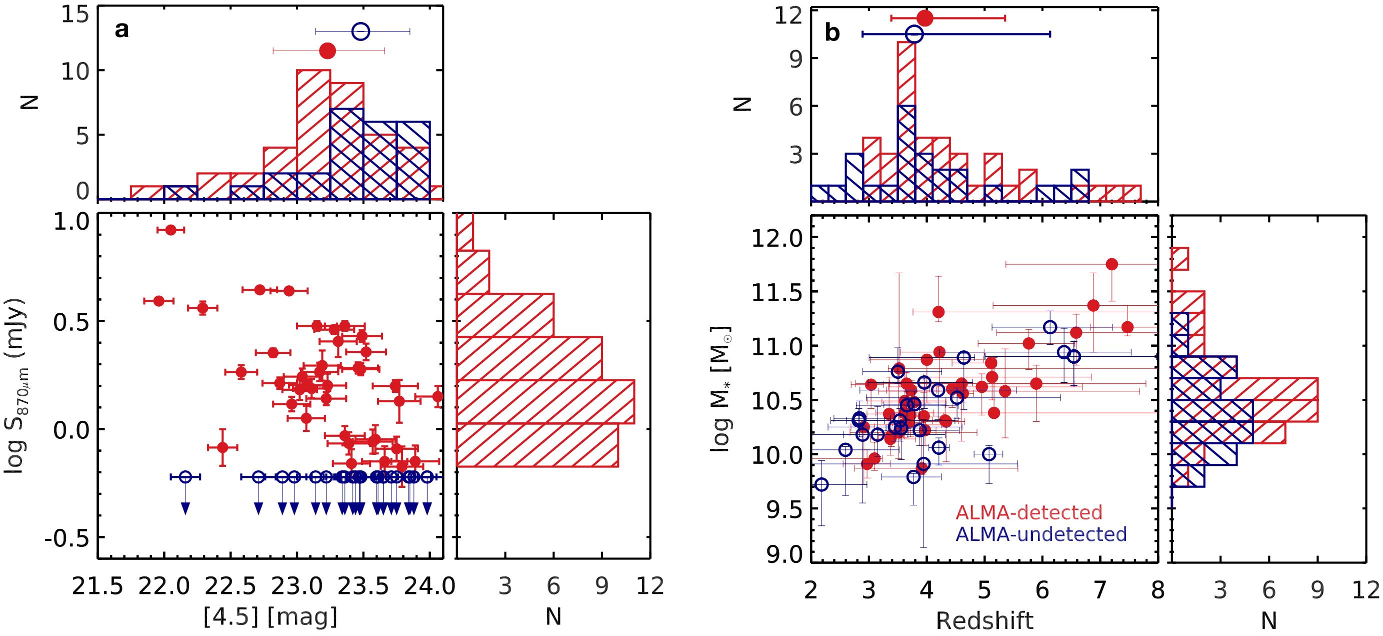

Extended Data Fig. 2 | Physical properties of ALMA-detected and ALMA-undetected *H*−dropouts. The ALMA-detected and un-detected *H*−dropouts are shown in blue and red, respectively. **a:** Main panel, the 870μm fluxes of ALMA-undetected H-dropouts are shown by their upper limits, $S_{870\mu m} < 0.6$ mJy (4σ). The ALMA-undetected H-dropouts tend to have slightly fainter 4.5 μm magnitudes, with a median value of $[4.5]_{\rm median} = 23.5$ compared to $[4.5]_{\rm median} = 23.2$ for ALMA-detected ones. The error bars for ALMA-detected H-dropouts denote their 1σ measurement error, while for ALMA-undetected H-dropouts their 4σ upper limits are shown. Top panel, histogram showing the distribution of the 4.5-μm magnitudes of H-dropouts. The filled and open circles and their error bars denote the median 4.5-μm magnitude as well as the 16th and 84th percentiles of ALMA-detected and undetected H-dropouts, respectively. Right panel, histogram showing the distribution of the 870-μm fluxes of ALMA-detected H-dropouts. **b:** Main panel, the redshift and stellar masses are derived by template-fitting of their optical-to-NIR photometry, as described in Methods. The ALMA-undetected H-dropouts tend to be at slightly lower redshifts and have lower stellar masses, with a median redshift of $z_{\rm med} = 3.8$ and stellar mass of $M_{*,\rm med} = 10^{10.31} M_\odot$ while the ALMA-detected ones have $z_{\rm med} = 4.0$ and $M_{*,\rm med} = 10^{10.56} M_\odot$. The error bars represent 1σ uncertainties as determined from our SED-fitting procedure (Methods). Top and right panels, histogram of the redshift and stellar mass distributions of H-dropouts, respectively. The filled and open circles and their error bars denote the median redshift as well as the 16th and 84th percentiles of the ALMA-detected and undetected H-dropouts, respectively.

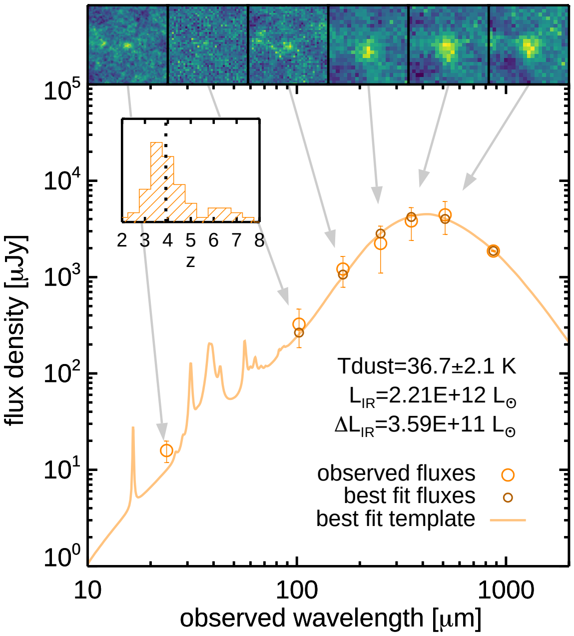

Extended Data Fig. 3 | Stacked far-infrared SED of ALMA-detected H-dropouts. The stacked IR SED is derived by median stacking of the Spitzer/24μm, Herschel/100μm, 160μm, 250μm, 350μm, 500μm, and ALMA 870μm images of the 39 H-dropouts detected with ALMA. The measured fluxes from the stacked images and predicted fluxes from the best-fit model (solid line) are shown with the large and small open circles, respectively. Error bars (1σ) on the stacked SED are obtained from either bootstrapping or from the statistics of the residual map (whichever is largest, as described and validated elsewhere[24]). For the ALMA photometry, the error bar is the formal error on the mean ALMA flux, and is smaller than the data point on this figure. The stacked images are shown in the row of insets at the top, which are linked to their corresponding stacked photometric points by grey arrows. The inset histogram shows the photometric redshift distribution of the H-dropouts based on optical-to-NIR SED fitting, which shows a median redshift of $z \approx 4$. The infrared luminosity $L_{\rm IR}$ and dust temperature $T_{\rm dust}$ are derived from the best-fit SED at $z = 4$, the average redshift of the sample, using an empirical IR SED library calibrated on galaxies at $0 < z < 4$ (ref. [13]). The uncertainty on the infrared luminosity ($\Delta L_{\rm IR}$) accounts for uncertainty on the photometry and on the dust temperature, but not on the mean redshift of the sample.

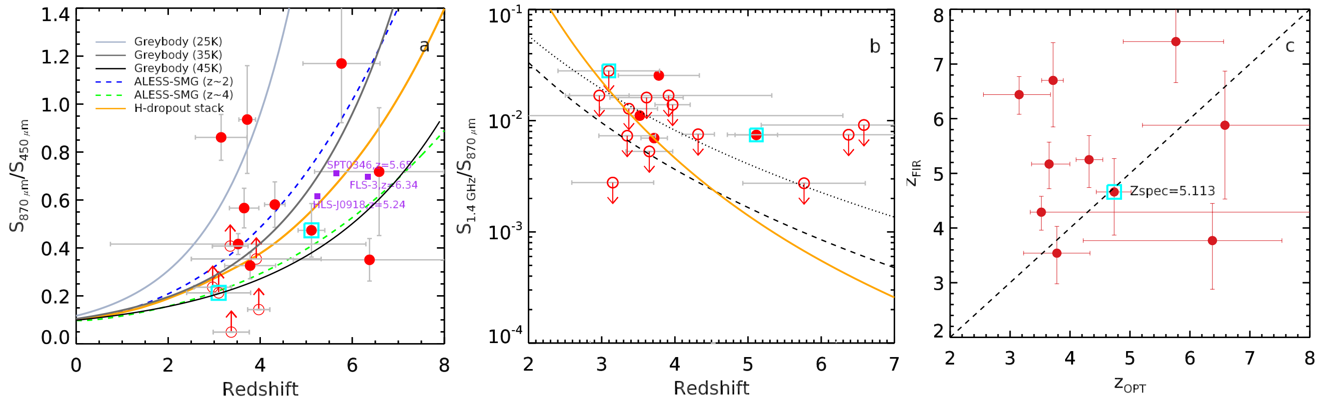

Extended Data Fig. 4 | Photometric redshifts of H-dropouts. **a**, **b**, $S_{870\ \mu m}/S_{450\ \mu m}$ (**a**) and $S_{1.4\ \rm GHz}/S_{870\ \mu m}$ (**b**) colors versus redshifts for ALMA-detected H-dropouts in CANDELS-COSMOS; **c**, comparison between redshifts derived from optical-to-NIR SEDs and from $S_{870\ \mu m}/S_{450\ \mu m}$ colors. **a**, The redshifts are photometric redshifts derived from optical-to-NIR SED fitting except for the two sources denoted in cyan squares, which are spectroscopic redshifts derived from X-SHOOTER spectra. The $S_{870\mu m}/S_{450\mu m}$ color for galaxies undetected at 450 μm (S/N < 2, open circles) are shown with their lower limits (using the 4σ upper limits at 450 μm). One of the spectroscopically confirmed galaxy with z_{spec}=3.097 is only marginally detected with $S_{870\mu m}$ = 0.4 ± 0.1 mJy, below our conservative detection limit, but we also include it here for illustration. The lines (see key) denote expected color evolution of different SED templates as a function of redshifts, including the stacked IR SED of the H-dropouts. We note that the $S_{870\ \mu m}/S_{450\ \mu m}$ color for both spectroscopically-confirmed sources are consistent with the average SED of ALESS $z = 4$ SMGs. A few previously spectroscopically confirmed bright SMGs at $z > 5$ are shown by purple squares[3,72,73]. **b:** The 1.4 GHz flux is derived from 3 GHz assuming a spectral index of $\alpha = -0.8$. A 3 σ upper limit of 7 μJy is assigned to non-detections at 3 GHz, which are shown with open circles. The dotted and dashed lines denote the relation between $S_{1.4\ \rm GHz}/S_{870\ \mu m}$ and redshifts for IR SEDs with spectral index in the submillimeter region of 3 (M82-like) and 3.5 (Arp220-like), respectively, as shown in ref. Carilli & Yun (1999)[74]. The same relation for the stacked IR SED of H-dropouts is also shown (orange line). **c:** Comparison between submillimeter redshifts ($z_{\rm FIR}$), derived on the basis of their $S_{870\ \mu m}/S_{450\ \mu m}$ color and their stacked IR SED (orange line in the left panel), and redshifts derived from optical-to-NIR SED fitting ($z_{\rm opt}$) for sources detected at both 450 μm and 870 μm. The cyan square denotes the source that is spectroscopically confirmed. Despite their large dispersion, both methods suggest that most of the H−dropouts are indeed at $z > 3$.

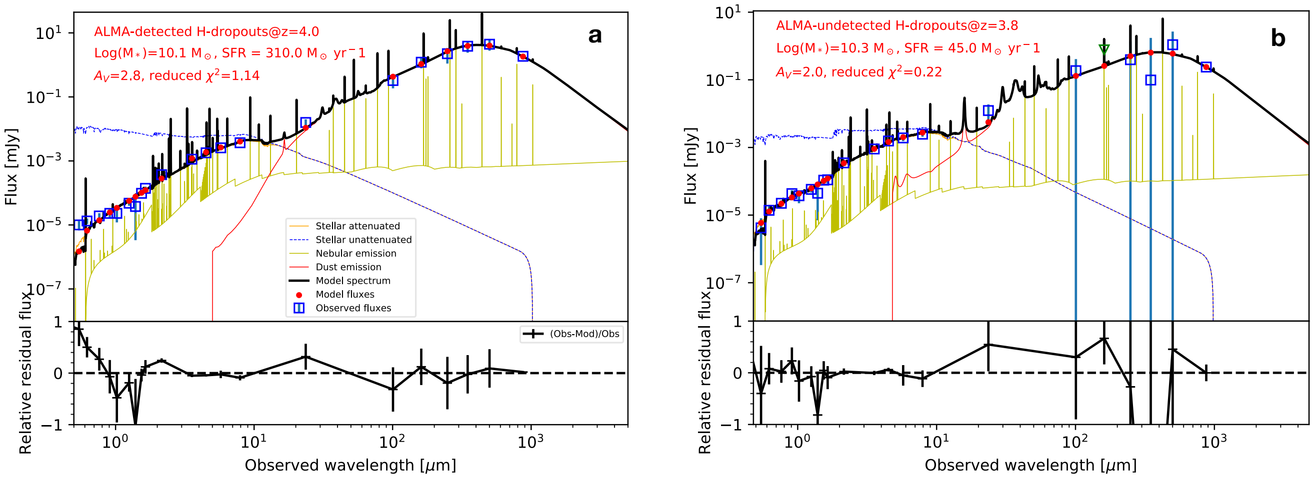

Extended Data Fig. 5 | Full best-fit model of the stacked SEDs of ALMA-detected and -undetected H-dropouts. a, ALMA-detected; **b**, ALMA-undetected. Here we show the best-fit SED templates obtained with the SED-fitting tool Cigale[75]. We have adopted the BC03[76] library of single stellar populations and delayed star formation history model, with Draine & Li [77] models for the dust emission. Nebular emission based on CLOUDY templates was also included[78]. ALMA-undetected H-dropouts have much lower specific SFR (sSFR) compared to that of ALMA-detected ones. Error bars show standard measurement error (1σ.

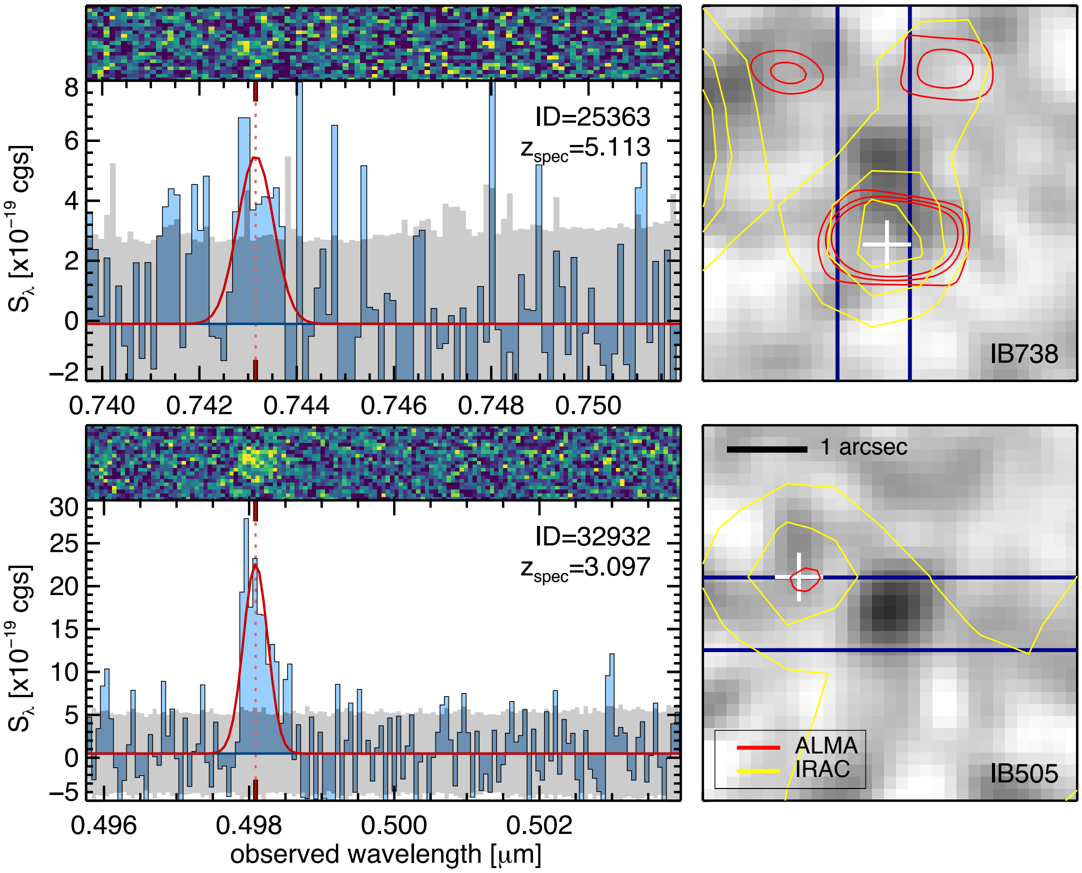

Extended Data Fig. 6 | X-SHOOTER spectra of two spectroscopically-confirmed H-dropouts. The two galaxies (with IDs 25363 and 32932) are shown on separate rows. Left, main panel, the observed spectra are shown on the left as black solid lines and blue shading, with uncertainties shown in the background as a gray shaded area. The best emission line model for Lyα is shown in red, and the centroid of the line is indicated with a vertical dotted line. The 2D spectrum is shown on the top, aligned with the 1D spectrum. Right, smoothed cutouts of the galaxies as observed on the Subaru medium band (IB738) where Lyα was detected. The X-SHOOTER slit is shown in blue, *Spitzer*–IRAC contours are shown in yellow, and ALMA contours are shown in red. The second galaxy with ID=32932 is only marginally detected with $S_{870\mu m}$ = 0.4 ± 0.1 mJy. The centroid of each dropout (determined from the IRAC image) is shown as a white cross.

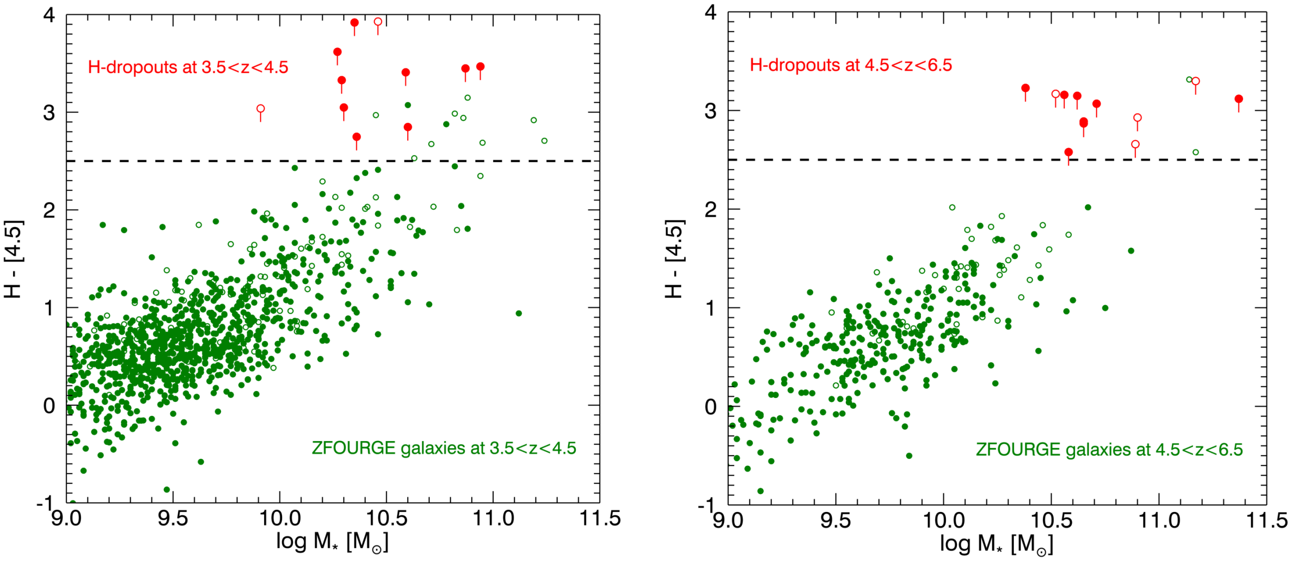

Extended Data Fig. 7 | $H - [4.5]$ color versus stellar mass for massive galaxies at $3.5 < z < 6.5$. Galaxies selected from the ZFOURGE catalog (left, $3.5 < z < 4.5$; right, $4.5 < z < 6.5$) with HST/F160W detections ($H < 27$) are shown in green while the H-dropouts selected in the same fields are shown in red. The $H - [4.5]$ color of the H-dropouts are shown by their lower limit assuming $H > 26.5(5\sigma)$. Quiescent and star-forming galaxies are shown by open and filled circles, respectively. Quiescent H−dropouts are defined as those undetected with ALMA while quiescent ZFOURGE galaxies are defined by their specific sSFR (based on SED fitting) with sSFR <0.3 Gyr^{-1} and no MIPS 24 μm detections [8].

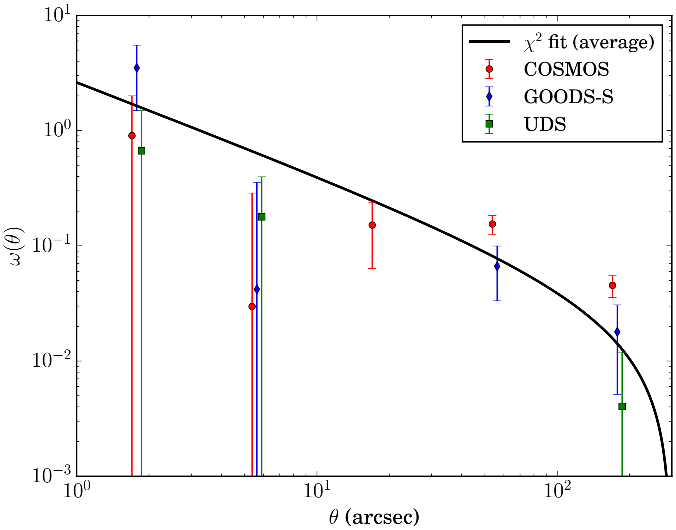

Extended Data Fig. 8 | Angular cross-correlation function between H-dropouts and UV-selected galaxies at $3.5 < z < 5.5$. The two-point angular cross-correlation function shown here, $\omega(\theta)$, is computed for the 39 ALMA-detected H-dropouts and ~6000 UV-detected (H-band) galaxies distributed in the same fields (CANDELS fields COSMOS, GOODS-S and UDS, see key). The solid black line is the best-fit line for the cross-correlation from the two-halo term (> 10″ scale). The error bars are estimated from Poisson statistics. See Methods for details.

Acknowledgements This paper makes use of the following ALMA data: ADS/JAO.ALMA#2015.1.01495.S, and ADS/JAO.ALMA#2013.1.01292.S. ALMA is a partnership of ESO (representing its member states), NSF (USA), and NINS (Japan), together with NRC (Canada), NSC, ASIAA (Taiwan), and KASI (Republic of Korea), in cooperation with the Republic of Chile. The Joint ALMA Observatory is operated by ESO, AUI/NRAO, and NAOJ. This paper makes use of JCMT data from programs M16AL006, MJLSC91, M11BH11A, M12AH11A, and M12BH21A. T. W. acknowledges the support by the NAOJ ALMA Scientific Research Grant Number 2017-06B, JSPS Grant-in-Aid for Scientific Research (S) JP17H06130, and funding from the European Union Seventh Framework Programme (FP7/2007-2013) under grant agreement No. 312725 (ASTRODEEP). X.S. acknowledges the support from NSFC 11573001, and National Basic Research Program 2015CB857005. C.-F.L. and W.-H.W. were supported by Ministry of Science and Technology of Taiwan Grant 105-2112-M-001-029-MY3.

Author Contributions T.W., C.S., and D.E. conceived the work, led the analysis and interpretation. T.W. proposed and carried out ALMA observations, reduced the ALMA data, measured SCUBA-2 fluxes and performed full SED fitting, and authored the majority of the text. C.S. conducted multiwavelength photometry and SED fitting, and carried out VLT/X-shooter observations and data reduction. Y.Yoshimura performed the clustering analysis. C.-F.L., W.-W.W. and X.S. contributed to the 450 μm photometry. K.K., Y. Yamaguchi, M.F., M.P., J.H., contributed to the overall interpretation of the results and various aspects of the analysis.

Code availability The codes used to reduce ALMA and X-shooter data are public available. The codes used to model the optical-to-infrared SEDs, and to stack the optical and infrared images are accessible through github (https://github.com/cschreib).

Data availability Source data for the ALMA 870μm imaging are available through the ALMA archive. Optical-to-infrared imaging for all the galaxies in the sample are also public available through HST and Spitzer data archive. The other data that support the plots within this paper and other findings of this study are available from the corresponding author upon reasonable request.

Author Information The authors declare that they have no competing financial interests. Correspondence and requests for materials should be addressed to T.W. (email: twang.nju@gmail.com,).